

Research
Laser Micro/Nano-Manufacturing—Article

Optically Reconfigurable Tamm Plasmonic Photonic Crystals for Visible Spectrum



Kuan Liu^a, Chuang Zheng^a, Shixin Gao^a, Xiaoming Chen^a, Shuang Zhang^{b,c,d}, Tun Cao^{a,*}

^aSchool of Optoelectronic Engineering and Instrumentation Science, Dalian University of Technology, Dalian 116024, China

^bNew Cornerstone Science Laboratory, Department of Physics, University of Hong Kong, Hong Kong 999077, China

^cDepartment of Electrical & Electronic Engineering, University of Hong Kong, Hong Kong 999077, China

^dMaterials Innovation Institute for Life Sciences and Energy (MILES), The University of Hong Kong Shenzhen Institute of Research and Innovation, Shenzhen 518052, China

ARTICLE INFO

Article history:

Received 19 July 2024

Revised 29 December 2024

Accepted 25 March 2025

Available online 28 March 2025

Keywords:

Tamm plasmon polaritons

Photonic crystals

Color display

Phase change materials

Tunable

ABSTRACT

Tamm plasmon polaritons (TPPs) are localized photonic states at the interface between a metal layer and one-dimensional (1D) photonic crystal substrate. Unlike surface plasmon polaritons (SPPs), TPPs can be excited by both transverse magnetic and electric waves without requiring additional coupling optics. TPPs offer robust color filtering, making them ideal for applications such as complementary metal oxide semiconductor (CMOS) image detectors. However, obtaining a large-area, reversible, and reconfigurable filter remains challenging. This study demonstrates a dynamically reconfigurable reflective color filter by integrating an ultrathin antimony trisulfide (Sb_2S_3) layer with Tamm plasmonic photonic crystals. Reconfigurable tuning was achieved by inducing Sb_2S_3 crystallization and reamorphization via thermal and optical activation, respectively. The material exhibited good stability after multiple switching cycles. The reflectance spectrum can be tuned across the visible range, with a shift of approximately 50 nm by switching Sb_2S_3 between its amorphous and crystalline phases. This phase transition is nonvolatile and substantially minimizes the energy consumption, enhancing efficiency for practical applications. Tamm plasmonic photonic crystals are low-cost and large-scale production, offering a platform for compact color display systems and customizable photonic crystal filters for realistic system integration.

© 2025 THE AUTHORS. Published by Elsevier LTD on behalf of Chinese Academy of Engineering and Higher Education Press Limited Company. This is an open access article under the CC BY license (<http://creativecommons.org/licenses/by/3.0/>).

1. Introduction

Surface plasmon polaritons (SPPs) are collective oscillations of electrons coupled with light waves on the surface of a metallic nanostructure [1,2]. Confined to subwavelength scales, SPPs significantly enhance light-matter interaction, enabling various nanophotonic applications [3–5]. Conventional SPPs feature a Gaussian-like resonance spectrum in the reflectance, transmittance, absorptance, and extinction spectra [6,7]. SPPs are useful for applications such as photodetection [8], solar energy conversion [9], photocatalysis [10], infrared imaging [11], filtering [12], quantum optics [13], and infrared astronomy [14]. Nanostructures or bulky coupling optical setups with prisms are commonly used to excite SPPs. Plasmonic nanostructures are often fabricated on a small scale using high-cost lithographic techniques such as electron beam lithography. Tamm plasmon polaritons (TPPs) can be excited

at the interface between a capping metal film and a one-dimensional (1D) photonic crystal (PhC) substrate [15–19], where incident photons are strongly localized at the interface [15]. TPP modes support a zero in-plane wave vector without requiring nanostructures or coupling optics [20]. Both the capping metal layer and 1D PhC substrate can be easily fabricated using established thin-layer deposition processes, making TPP crystals (TPPCs) scalable for large photonic devices, such as *in situ* color displays and electronic signage devices [21]. Particularly, TPPCs may enable the realization of vivid structural colors in the transmittance and reflectance spectra across the visible spectrum. However, few studies have explored this possibility.

TPPCs are typically a “fixed-by-design,” meaning that the colors are statically written into the surface [22], and once fabricated, their optical characteristics remain unchanged. This static nature limits their applications, as real-time changes in displayed images or information are essential for maximizing their potential. Therefore, dynamic color modulation is desirable in dynamic color display systems [23]. However, actively reconfigurable TPPCs have not yet been

* Corresponding author.

E-mail address: caotun1806@dlut.edu.cn (T. Cao).

explored for the reversible tuning of the TPP modes. Although recent studies [24–27] have investigated the active tuning of TPPs, their use in generating reconfigurable high-purity structural colors remains underdeveloped. Recently, dynamically tunable structural coloring has been achieved by integrating various dielectric layers, including electroactive conducting polymers [28], tungsten oxide [29], floating solid-state thin films [30], and phase-change materials (PCMs) [23,31], into thin-film optical coatings. These innovations have attracted significant interest owing to their scalability, cost-effectiveness, and elimination of lithography in nanofabrication processes. Typically, thin-film coatings consist of dielectric-metal multilayers that generate colors through selective light absorption. However, these conventional dielectric-metal coatings have limitations, including poor color purity and the production of iridescent colors in both reflection and transmission modes.

Chalcogenide PCMs, such as the well-known transition metal chalcogenide alloy Ge–Sb–Te (GST), are highly transparent in the near- to far-infrared regions. These materials exhibit large and reversible permittivity modulation upon crystallization, making them suitable for applications such as spectrally efficient filtering and imaging [32–35]. However, GST alloys exhibit relatively large losses and minimal changes in refractive index in the visible spectrum, limiting their application in color display technologies [36,37]. Recently, antimony trisulfide (Sb_2S_3), another chalcogenide alloy, has emerged as a promising material for visible-light photonic applications owing to its large index contrast of approximately 1 and significantly lower losses in the visible spectrum compared with GST [38]. Sb_2S_3 -integrated heterostructures have been applied in color nanoprints [31] and solar cell devices [39]. However, few studies have explored the use of Sb_2S_3 for tunable TPPCs in the visible region, which can enable accurate switchable structural color by selectively reflecting visible light.

This study presents reconfigurable visible-light spectral filters utilizing Sb_2S_3 -integrated TPPCs with dynamic tuning and reversible operations in the reflectance spectrum. The TPP resonance could be tuned by varying the thickness of the Sb_2S_3 layer to selectively absorb the blue, green, and yellow spectral bands. This results in vivid, nonvolatile colors, such as yellow, fuchsia, and blue. By switching the Sb_2S_3 layer from its amorphous (AM) to crystalline (CR) state using ultrafast (nanosecond) pulsed lasers and heat-induced phase transitions, the resonance shifts by 50 nm. A print of the “seven-color flower” pattern is demonstrated by using the stepwise TPPCs, where the pattern’s color is dynamically varied through the reversible state transition of Sb_2S_3 . Notably, these TPPCs can be fabricated without requiring complex lithographic techniques, simplifying the fabrication process and reducing device cost. Unlike traditional tunable thin-film optical coatings [23,28–31], our TPPCs exhibit a narrow full width at half maximum (FWHM) in the visible spectral range, enabling precise and vivid color filtering [40,41]. Notably, our results demonstrate that the Sb_2S_3 -based TPPCs exhibit exceptional stability over multiple cycles in both AM and CR states, marking a unique advancement in this field. Moreover, their nonvolatile nature significantly reduces energy consumption. Our planar Sb_2S_3 -integrated TPPCs platform represents progress in developing reversibly tunable spectral filters with applications in erasable inkless paper and camouflaging surfaces for visible light.

2. Materials and methods

2.1. Sample fabrication

2.1.1. Materials deposition

A 500 μm thick Si wafer was used as the substrate and cleaned with acetone, isopropyl alcohol, and deionized water in an ultra-

sonicator. A five-layer stack of silicon dioxide and zinc sulfide (SiO_2/ZnS) films was deposited onto the substrate. The individual thicknesses of the SiO_2 and ZnS layers were 85 and 53 nm, respectively, using radio frequency (RF) magnetron sputtering at 20 °C. The RF sputtering power applied for both SiO_2 and ZnS was set at 100 W. Subsequently, a 10-nm-thick Sb_2S_3 film was deposited on the SiO_2/ZnS stacked layers via RF sputtering at 20 °C, with 6.67×10^{-5} Pa chamber base pressure and 30 W power. We employed a deposition rate of 0.5 $\text{\AA}\cdot\text{min}^{-1}$, using an Sb_2S_3 alloy target (99.9% purity, 50.8 mm diameter) in an argon (Ar) atmosphere. Finally, a 15-nm-thick Ag film was deposited onto the Sb_2S_3 layer using direct current (DC) sputtering.

2.1.2. Photolithography

The photoresist was exposed to determine the color pattern, as shown in “seven-color flower” on the Sb_2S_3 film, using a double-sided mask aligner system (MA6–BSA, Suss MicroTec, Germany). Subsequently, the photoresist was developed in a 1:6 mixture of AR 300–26 (Allresist GmbH, Germany) and deionized water, followed by rinsing with deionized water. Sb_2S_3 and Ag films were deposited on the SiO_2/ZnS stacked layers. Liftoff was applied in acetone to form the petals. These steps were repeated to fabricate a seven-color flower pattern.

2.2. Sample measurements

2.2.1. Reflectance spectra

Reflectance spectra of the Sb_2S_3 -based TPPCs displays on the Si substrate were measured using a Fourier-transform infrared (FTIR) spectrometer (IFS; 66 $\text{v}\cdot\text{s}^{-1}$) integrated with a Bruker microscope (Hyperion 2000, Bruker, Germany). The data were recorded over the spectral region from 25 000 to 9000 cm^{-1} with a 1 cm^{-1} spectral resolution. A 15 \times objective lens and Si detector were employed to collect data in the reflectance mode. The scanner velocity was set to 20 kHz, and interferograms were Fourier-transformed using a Blackman–Harris three-term apodization function and a zero-filling factor of 4. All FTIR spectra were normalized by dividing measured spectra by the background spectrum of a bare 100 nm Ag film on a Si substrate, yielding the reflectance ratio. FTIR spectroscopy was performed at 20 °C with a relative air humidity of 20%. Angle-resolved reflectance spectra were obtained using variable-angle high-resolution spectroscopic ellipsometry, which can collect data over the spectral region (400–750 nm). The incident angle varied from 20° to 80°.

2.2.2. Refractive index measurement

The complex refractive index of Sb_2S_3 in both AM and CR phases was measured using a J.A. Woollam ellipsometer, fitted with Tauc-Lorentz oscillator models. The incident wavelength ranged from 400 to 750 nm, with a spectroscopic resolution of 5 nm. Measurements were taken at incident angles of 65° and 75° at room temperature with a relative air humidity of 20%. Precise ellipsometry required meticulous calibration of the parameters, which was achieved using a multi-sample regression calibration procedure [42].

2.3. Numerical simulation

Simulations were conducted using the finite-difference time-domain (FDTD) method in Lumerical Solutions software (Lumerical Solutions, Canada). A periodic boundary condition was applied in the x – y plane, and the simulation area along the z -axis was defined using perfectly matched layer boundary conditions. The TPPCs were vertically illuminated using a plane wave propagating along the $-z$ direction. Reflectance data were collected via a power monitor placed 1 μm above the TPPCs structure. A cubic Yee cell with

$\Delta x = \Delta y = \Delta z = 2 \text{ nm}$ (Δx , Δy , and Δz are the mesh sizes along the x , y , and z directions, respectively) and a time step $\Delta t = 1 \times 10^{-18} \text{ s}$ were employed [43]. The mesh sizes were sufficiently small to minimize numerical errors and ensure convergence of the electric (E)-field intensities around the resonant antenna. Sb_2S_3 was incorporated in the numerical models using the measured complex permittivity, as shown in Fig. S1 in Appendix A.

2.4. Experimental realization of the Sb_2S_3 reversible state transition

A reconfigurable color display was achieved by inducing Sb_2S_3 crystallization and reamorphization via thermal and optical activations, respectively. In this study, a high-repetition-rate nanosecond laser was used to convert the state of an Sb_2S_3 film from CR to AM. The laser parameters are as follows: 1064 nm wavelength, 200 kHz repetition rate, 100 ns pulse width, and 10 μm spot diameter. Particularly, to re-amorphize the CR Sb_2S_3 film, an average laser power of 150 mW and a stage movement velocity of 50 $\text{mm}\cdot\text{s}^{-1}$ were employed, increasing the local temperature promptly beyond 801 K to melt the Sb_2S_3 . Subsequent fast cooling quenched the melted layer to the AM state. The AM Sb_2S_3 film was subsequently crystallized by thermally annealing the TPPCs for 2 min at $T_d = 543 \text{ K}$ on a hotplate in an Ar atmosphere. This temperature T_d is between crystallization temperature ($T_c = 505 \text{ K}$) and melting temperature ($T_m = 801 \text{ K}$), which changes the structural phase from as-deposited-AM (AD-AM) to CR.

3. Results and discussion

Fig. 1(a) shows a schematic of the reconfigurable TPPCs integrated with an Sb_2S_3 film with an encapsulated Ag monolayer on top of the TPPCs structure. The structure is supported by a Si substrate. The

TPPCs consisted of a distributed Bragg reflector (DBR) with five SiO_2/ZnS double layers. The thicknesses of the Ag, SiO_2 , and ZnS layers were fixed at 15, 85, and 53 nm, respectively. A silver film was selected as the metal capping layer owing to its outstanding plasmonic performance in the visible spectrum and compatibility with standard semiconductor manufacturing processes [22]. The proposed Sb_2S_3 -based TPPCs generated the desired color in the AM state by adjusting the thickness of the Sb_2S_3 layer to control the resonant absorption. When the Sb_2S_3 layer transitioned to the CR state, its index change shifted the resonant absorption spectrum, leading to a slight color change, as shown in Fig. 1(a).

A cross-sectional focused ion beam (FIB) image of a TPPC with a 10 nm thick Sb_2S_3 is depicted in Fig. 1(b), and the corresponding FTIR measured reflectance spectra in both AM and CR states are illustrated in Fig. 1(c). Incident light can be efficiently coupled to the Tamm plasmon resonance mode, leading to significantly low reflectance at the resonant frequency. In the AM state, the resonance, as indicated by the reflection dip, occurred at wavelength $\lambda = 530 \text{ nm}$, corresponding to the green spectral band, yielding a “fuchsia” color. By heating the TPPCs structure for 2 min at $T_d = 543 \text{ K}$ on a hotplate in an Ar atmosphere, the Sb_2S_3 layer experienced a structural phase from as-AD-AM to CR, and the resonant absorption shifted to 560 nm due to the index change, resulting in a “blueviolet” color. The Sb_2S_3 layer thickness decreased by approximately 10% during the transition from AM to CR, corresponding to an increase in Sb_2S_3 density upon crystallization [44,45]. As seen in Fig. S2 in Appendix A, this reduction effect resulted in only a minor shift of approximately 2 nm in resonant absorption. In Fig. 1(d), FDTD simulated reflectance simulation results of the reflection spectrum of the designed structure aligned with measurements in both reflectance $R(\omega)$ spectra and colors, showing that the change of permittivity induced by state transition

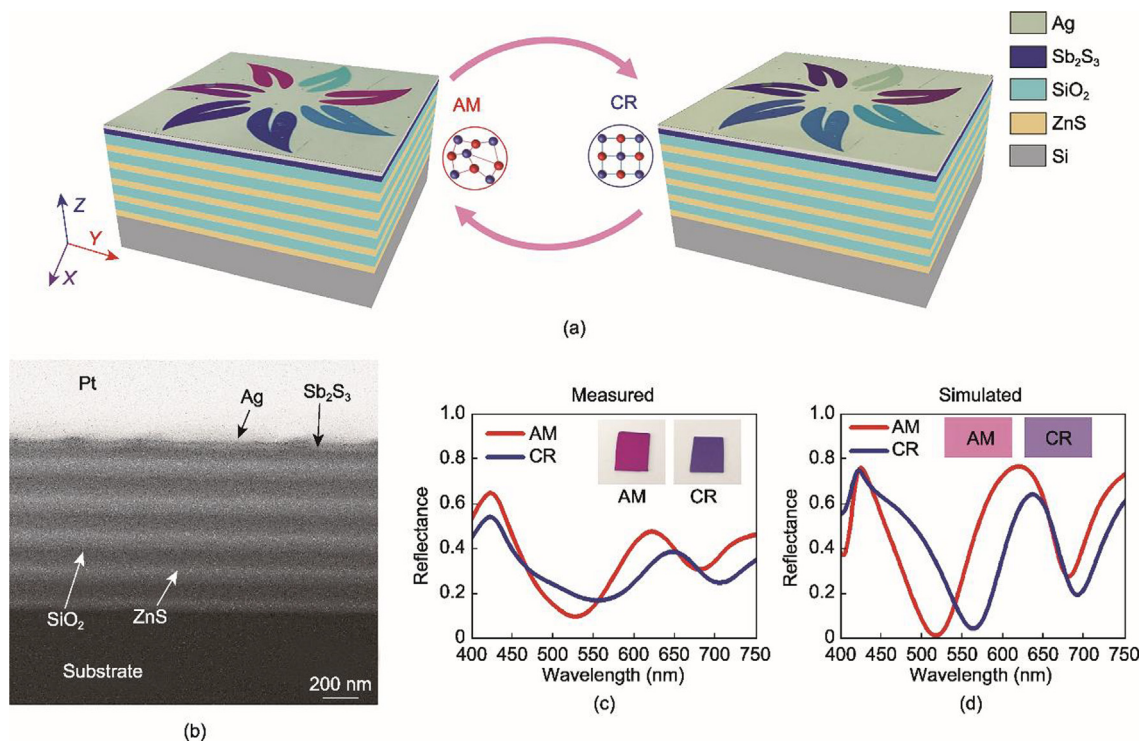


Fig. 1. Configuration of the TPPCs-based color display. (a) Schematic of the reversibly tunable TPPCs-based color display. The thicknesses of the Ag capping layer, Sb_2S_3 phase change layer, and each film of five pairs of SiO_2/ZnS stacks were $T_{\text{Ag}} = 15 \text{ nm}$, $T_{\text{SbS}} = 10 \text{ nm}$, $T_{\text{SiO}} = 85 \text{ nm}$, and $T_{\text{ZnS}} = 53 \text{ nm}$, respectively. The entire TPPCs structure was deposited onto a Si substrate with a thickness of 500 μm . Inset: structural state change between the AM and CR states. (b) A cross-sectional FIB image of the TPPCs structure. (c) The FTIR measured and (d) FDTD simulated reflectance of the TPPCs for the AM and CR states. The insets in (c) and (d) show the photomicrographs and colorimetric calculations of the TPPCs in the AM and CR states, respectively.

led to the color alternation in the structure. The discrepancies between the experimentally measured and numerically simulated data were primarily due to surface roughness and structural imperfections during the thin film deposition [46,47] and Sb_2S_3 degradation [44,45]. In Fig. S3 in Appendix A, the reflectance of the TPPCs was measured 10 times, with the average reflectance spectrum calculated for both AM (Fig. S3(a)) and CR states (Fig. S3(b)). The zoomed-in view (right column) reveals a measurement error range of 2% to 4%, with the black squares and error bars representing the average and standard deviation of 10 successive measurements, respectively. This minimal error was unlikely to have a significant impact on the color palette coverage or standard red green blue (sRGB) gamut. This issue was attributed to the FTIR measurements. Random errors in reflectance measurements were influenced equally by uncertainties in the determination of the temperature profile, errors in defining the spectral zero line, and random noise inherent in spectroscopic measurements. This measurement noise can be minimized by averaging the data over multiple measurements.

A reamorphization of Sb_2S_3 (from CR to melting-quenched AM (MQ-AM)) can be achieved by annealing the sample above its melting temperature (T_m) using high-intensity pulses with short periods to melt the crystal lattice [48,49], followed by rapid

quenching to “freeze” the AM phase at a rate of 10^9 to $10^{10} \text{ K}\cdot\text{s}^{-1}$ [50]. The reversible structural transition is schematically shown in Fig. S1(a). Fig. 2(a) shows five complete state-transition switching cycles, with resonance peak positions recorded to demonstrate the stability of the reversal characteristics. In Fig. 2(b), we show that the TPPCs exhibit outstanding stability over all cycles in both the AM and CR states. The spectral response profile of each state remains constant, with no observable hysteresis.

We examined the configuration where a high-refractive-index Sb_2S_3 layer was positioned adjacent to a metal layer to facilitate the generation of TPPs. To further investigate the generation mechanism of TPPs, we calculated the complex reflection coefficients r_{Ag} and r_{PhC} for the Ag film and the PhC, respectively. For AM Sb_2S_3 , the condition $\text{Arg}[r_{\text{Ag}} r_{\text{PhC}} \exp(2i\varphi)] \approx 0$ (i is the imaginary unit) was satisfied at approximately 530 nm, where φ represents the phase of the light propagating through the Sb_2S_3 layer. This wavelength corresponds precisely to the position of the reflection dip, as shown in Fig. 1(c). Given that both the Ag film and the PhC exhibited highly reflective properties ($|r_{\text{Ag}}|, |r_{\text{PhC}}| \approx 1$), the structure met the excitation condition for TPPs: $r_{\text{Ag}} r_{\text{PhC}} \exp(2i\varphi) \approx 1$ [15,51,52]. Fig. 3 illustrate the numerical distributions of E -field at the two TPP resonance wavelengths of $\lambda_1 = 530 \text{ nm}$ and $\lambda_2 = 560 \text{ nm}$ for the AM and CR states, respectively (see the detailed discussion in

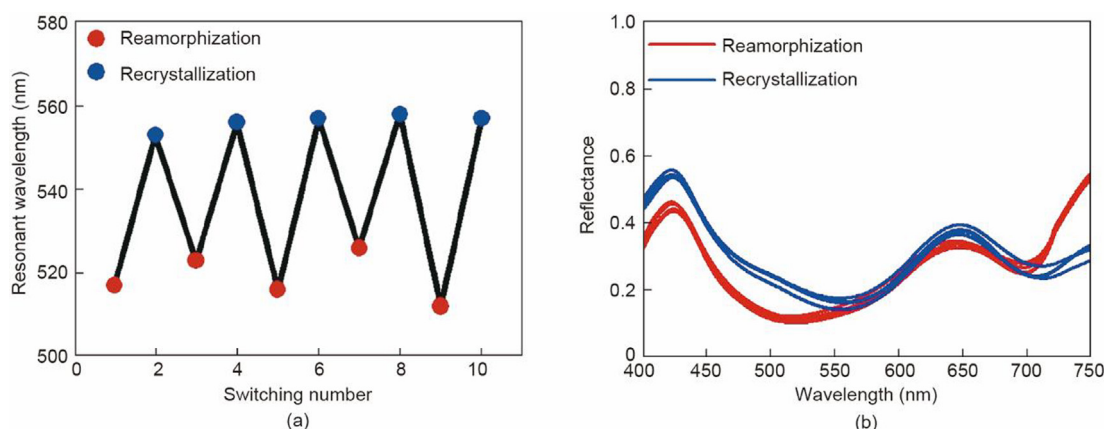


Fig. 2. Stability of reconfigurability can be maintained across a few switching cycles. In the reversible state transition, nanosecond laser pulses were used to reamorphize the CR Sb_2S_3 by heating it above 801 K, followed by rapid quenching. Recrystallization of the AM Sb_2S_3 film was achieved using a hot plate, which heated the film above 543 K but below 801 K. (a) Reflectance resonant central wavelength (valley) as a function of switching number. (b) Cyclability measurement reflectance for the device.

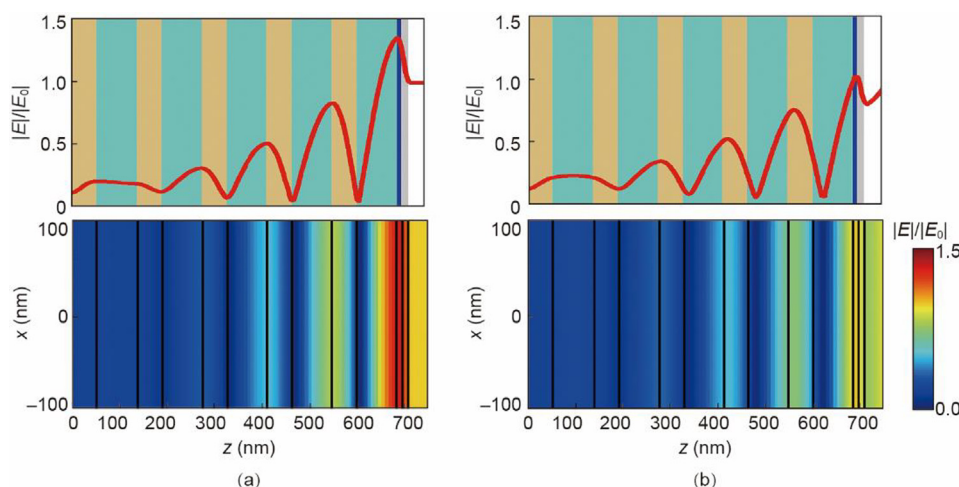


Fig. 3. Distributions of E -field at the TPP resonance wavelengths of $\lambda_1 = 530 \text{ nm}$ and $\lambda_2 = 560 \text{ nm}$ for the (a) AM and (b) CR states, respectively. $|E|$ represents the absolute magnitude of the local electric field with the structure, and $|E_0|$ represents the incident field without structure.

the Section 2.3). In both cases, the *E*-field decayed exponentially from the Ag/DBR interface to the Bragg structure, which is a typical characteristic of Tamm modes [53–56]. Fig. S4 in Appendix A shows the *E*-field distributions at the resonance dip of $\lambda_3 = 677$ nm in the AM state. Notably, at $\lambda_3 = 677$ nm, the light wave energy was primarily concentrated within the SiO₂ layer of the DBR, adjacent to the Si substrate. This resonance eigenmode at $\lambda_3 = 677$ nm corresponds to a Fabry–Perot (FP) mode, confined between the Ag film and the Si substrate, with the DBR acting as an isolated optical cavity [56]. The FP mode sustained a strong resonance of the *E*-field confined within the cavity formed by the Ag film and Si mirror. The simulated reflectance spectra are presented for pristine DBR and DBR coated with Sb₂S₃ in the AM and CR phases in Fig. S5 in Appendix A. The results revealed that incorporating Sb₂S₃ induced a distortion in the red-side fringe of the DBR reflectance spectrum. However, the phase transition of Sb₂S₃ from the AM state to the CR state did not result in a significant spectral shift.

The angular dependence of the reflection spectrum is crucial for display applications. Figs. 4(a) and (b) illustrate the angle-resolved reflectance spectra of the TPPC in both AM and CR states for unpolarized incidence. By increasing the incident angle (θ_i) from 20° to 80°, the TPPCs reflector exhibited a near-zero reflectance of $R(\omega) = 0.05$ at approximately $\lambda_1 = 530$ nm for the AM state. The angle-resolved reflectance spectrum was red-shifted by changing the state from AM to CR. Additionally, these measurements showed a blueshifted reflectance dip with increasing θ_i , consistent with numerical simulation in Fig. S6 in Appendix A. Fig. 4(c) shows optical images of the TPPCs reflector in the AM state at varying viewing angles up to 80°. The structure’s color remained stable for viewing angles between 0° and 50° but changed to green at 80° due to decreased reflection intensity. However, the peak positions of the reflectance spectra remained largely unchanged across viewing angles ranging from 0° to 50°. This instability indicates the absence of significant color variation when the TPPCs are viewed from different angles [57]. Consequently, these results confirm that the color properties of our design are insensitive to both the incidence angle (ranging from 0° to 50°) and the polarization [58].

Our device demonstrates a vivid reflective color with high purity and luminance across a broad angular range of up to $\pm 50^\circ$, regardless of the incident light’s polarization or direction. Our approach holds significant potential for applications such as colored displays and image sensors.

By gradually increasing the thickness of the Sb₂S₃ phase change layer T_{SbS} film from 10 to 25 nm, a complete color palette spanning the entire visible spectrum was achieved, as depicted in the left column of Fig. 5(a). The corresponding reflectance dip shifted from 530 to 620 nm in the AM state (solid lines) and from 562 to 652 nm in the CR state (dashed lines). The measured colors of the TPPCs with various thicknesses are shown in the right column of Fig. 5(a). In the AM state, the TPPCs exhibited yellow, fuchsia, purple, blue, and cyan colors for different thicknesses of T_{SbS} . In the CR state, the corresponding TPPCs underwent considerable color changes. In Fig. 5(b), we mapped the corresponding color points on the Commission Internationale de l’Éclairage (CIE) chromaticity diagram, which quantified the color distributions for both the AM and CR phases. By increasing the T_{SbS} from 3 to 30 nm, the samples in both the AM and CR phases occupied a considerable gamut within the color space of sRGB. A significant difference in color was observed between the AM and CR phases. The measured color palettes of the TPPCs are shown in Fig. 5(c). The numerically simulated spectra for samples of different thicknesses and in both the AM and CR states, presented in Fig. S7 in Appendix A, closely matched the experimental results. A database was then constructed using the measured palette colors shown in Fig. 5(c), linking the RGB values with the Sb₂S₃ layer deposition thickness. Different colors can be produced in various sections by modifying the magnetron sputtering deposition time.

Finally, photolithography was used to define a colored pattern on the sample (Fig. 6). This technique was demonstrated with fuchsia flower patterns on the Ag/Sb₂S₃ dual layers in the AM state. By switching the sample to the CR state, the color of the “Flower” was varied from fuchsia to blue–violet, as shown in Fig. 6(a). Additionally, a multicolor pattern was achieved, as shown in Fig. 6(c). Specifically, a “seven-color flower” was formed in the AM state.

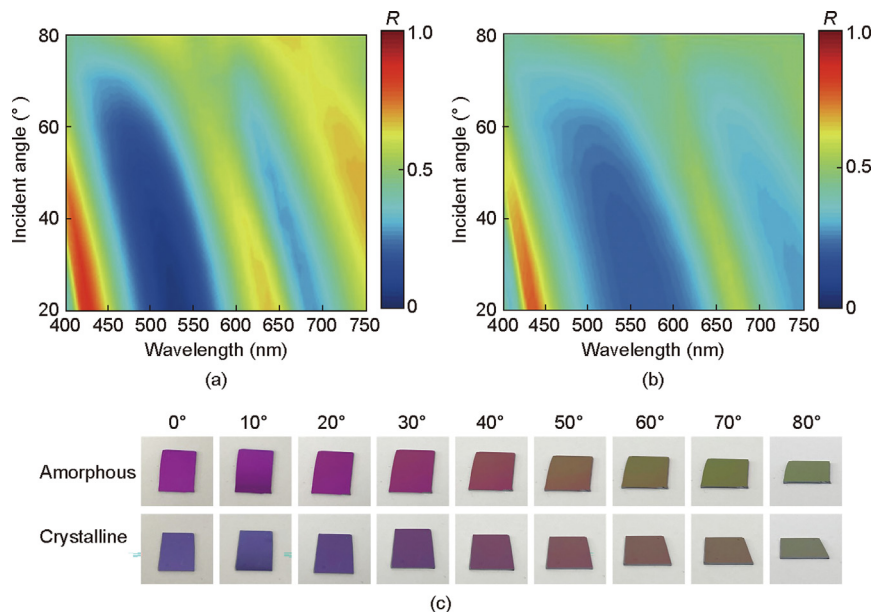


Fig. 4. Variable angle spectroscopic ellipsometry (VASE) measurement of incident angle-resolved reflectance spectra for the Sb₂S₃-based TPPCs for both (a) AM and (b) CR phases. *R*: reflectance. (c) Optical images of AM and CR TPPCs at the different observation angles. The sample’s size is 1.2 cm × 1.5 cm.

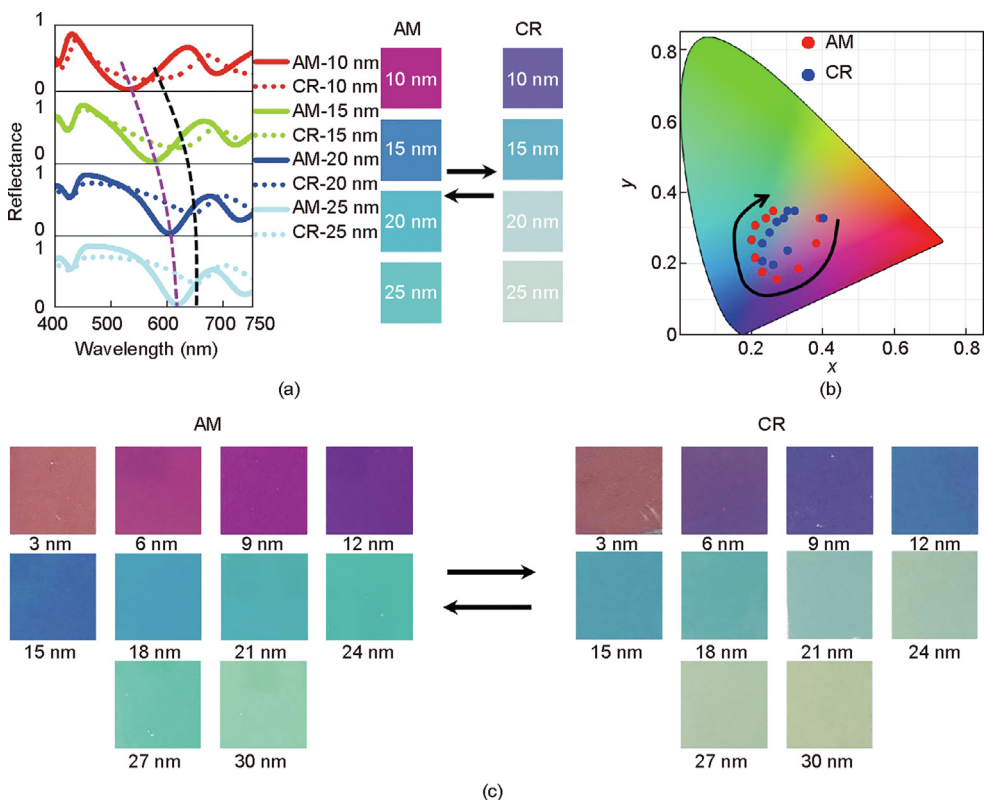


Fig. 5. (a) Experimentally measured reflectance (left column) and colors (right column) of the four TPPCs structures with T_{SbS} = 10, 15, 20, and 25 nm, for both AM and CR states, respectively. (b) Color coordinates from the measured spectra on the CIE 1931 chromaticity figure of TPPCs as increasing the T_{SbS} from 3 to 30 nm according to arrow direction. (c) Color palettes of the TPPCs with AM (left column) and crystalline (right column) phases as varying the T_{SbS} from 3 to 30 nm.

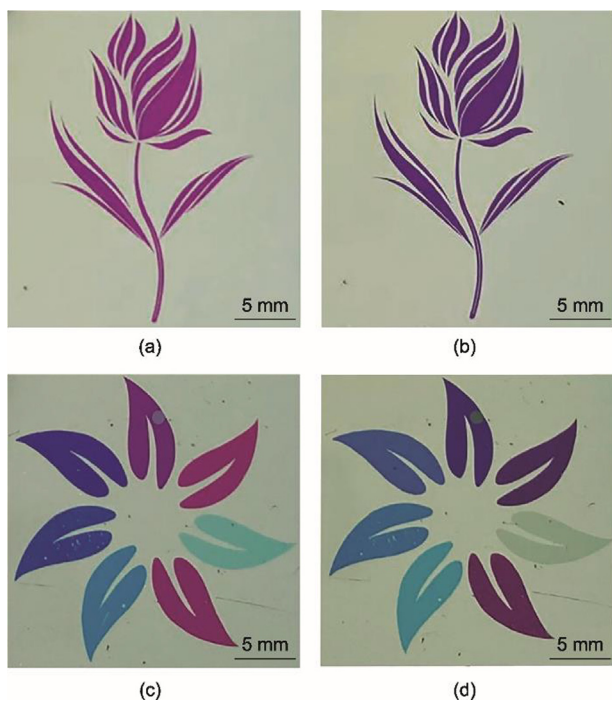


Fig. 6. Optical images of the fabricated "Flower" display with (a) AM and (b) CR states. The optical images of the fabricated "seven-color flower" with (c) AM and (d) CR states.

Fig. 6(d) shows a radical color change when transitioning the state from the AM to the CR state.

4. Conclusions

This study demonstrated a fully reconfigurable Sb_2S_3 -based TPPCs color display that operates across the visible spectrum by exploring the state transition of Sb_2S_3 between AM and CR states. This color-displaying structure explores the large change in permittivity caused by the phase change in Sb_2S_3 between AM and CR states. By adjusting the laser power, a reversible phase transition was confirmed by measuring the complex refractive index and reflectance spectra. Using nanosecond laser pulses and thermal heating, the TPPCs were dynamically tuned to selectively reflect different interference colors, with reversible cycling achieved via structural phase transitions in Sb_2S_3 . Additionally, magnetron sputtering was employed to fabricate diverse color images in the same TPPCs region using the state transitions in Sb_2S_3 . This approach offers advantages such as being lithography-free, nonvolatile, fast, and low-cost, with potential applications in next-generation near-eye displays and high-resolution optical encryption devices.

CRediT authorship contribution statement

Kuan Liu: Validation. **Chuang Zheng:** Data curation. **Shixin Gao:** Formal analysis. **Xiaoming Chen:** Visualization. **Shuang Zhang:** Data curation. **Tun Cao:** Writing – original draft, Supervision, Conceptualization.

Declaration of competing interest

The authors declare that they have no known competing financial interests or personal relationships that could have appeared to influence the work reported in this paper.

Appendix A. Supplementary data

Supplementary data to this article can be found online at <https://doi.org/10.1016/j.eng.2025.03.025>.

References

- [1] Brongersma ML, Shalaev VM. The case for plasmonics. *Science* 2010;328(5977):440–1.
- [2] Zayats AV, Smolyaninov II, Maradudin AA. Nano-optics of surface plasmon polaritons. *Phys Rep* 2005;408(3–4):131–314.
- [3] Homola J, Yee SS, Gauglitz G. Surface plasmon resonance sensors: review. *Sens Actuators B* 1999;54(1–2):3–15.
- [4] Kabashin AV, Patskovsky S, Grigorenko AN. Phase and amplitude sensitivities in surface plasmon resonance bio and chemical sensing. *Opt Express* 2009;17(23):21191–204.
- [5] Ndukaike JC, Mishra A, Guler U, Nnanna AGA, Wereley ST, Boltasseva A. Photothermal heating enabled by plasmonic nanostructures for electrokinetic manipulation and sorting of particles. *ACS Nano* 2014;8(9):9035–43.
- [6] Kretschmann E, Raether H. Notizen: radiative decay of non radiative surface plasmons excited by light. *Z für Naturforschung A* 1968;23(12):2135–6.
- [7] Otto A. Excitation of nonradiative surface plasma waves in silver by the method of frustrated total reflection. *Z Physik* 1968;216(4):398–410.
- [8] Salamin Y, Ma P, Baeuerle B, Emboras A, Fedoryshyn Y, Heni W, et al. 100 GHz plasmonic photodetector. *ACS Photonics* 2018;5(8):3291–7.
- [9] Kamat PV, Hartland GV. Plasmons for energy conversion. *ACS Energy Lett* 2018;3(6):1467–9.
- [10] Lim SY, Law CS, Bertó-Roselló F, Liu L, Markovic M, Ferré-Borrull J, et al. Tailor-engineered plasmonic single-lattices: harnessing localized surface plasmon resonances for visible-NIR light-enhanced photocatalysis. *Catal Sci Technol* 2020;10(10):3195–211.
- [11] Franklin D, Modak S, Vázquez-Guardado A, Safaei A, Chanda D. Covert infrared image encoding through imprinted plasmonic cavities. *Light Sci Appl* 2018;7(1):93.
- [12] Xu T, Wu YK, Luo XG, Guo LJ. Plasmonic nanoresonators for high-resolution colour filtering and spectral imaging. *Nat Commun* 2010;1(1):59.
- [13] Akimov A, Mukherjee A, Yu C, Chang D, Zibrov A, Hemmer P, et al. Generation of single optical plasmons in metallic nanowires coupled to quantum dots. *Nature* 2007;450(7168):402–6.
- [14] Tyo JS, Goldstein DL, Chenault DB, Shaw JA. Review of passive imaging polarimetry for remote sensing applications. *Appl Opt* 2006;45(22):5453–69.
- [15] Kaliteevski M, Iorsh I, Brand S, Abram R, Chamberlain J, Kavokin A, et al. Tamm plasmon-polaritons: possible electromagnetic states at the interface of a metal and a dielectric bragg mirror. *Phys Rev B* 2007;76(16):165415.
- [16] Gazzano O, de Vasconcellos SM, Gauthron K, Symonds C, Bloch J, Voisin P, et al. Evidence for confined Tamm plasmon modes under metallic microdisks and application to the control of spontaneous optical emission. *Phys Rev Lett* 2011;107(24):247402.
- [17] Wu J, Qing YM. Strong nonreciprocal radiation with topological photonic crystal heterostructure. *Appl Phys Lett* 2022;121(11):112201.
- [18] Qing YM, Ma HF, Cui TJ. Flexible control of light trapping and localization in a hybrid Tamm plasmonic system. *Opt Lett* 2019;44(13):3302–5.
- [19] Wu J, Wang Z, Wu B, Shi Z, Wu X. The giant enhancement of nonreciprocal radiation in Thue–Morse aperiodic structures. *Opt Laser Technol* 2022;152:108138.
- [20] Sasin ME, Seisyan RP, Kalitchevski MA, Brand S, Abram RA, Chamberlain JM, et al. Tamm plasmon polaritons: slow and spatially compact light. *Appl Phys Lett* 2008;92(25):251112.
- [21] Jeng SC. Applications of Tamm plasmon-liquid crystal devices. *Liq Cryst* 2020;47(8):1223–31.
- [22] Carrillo SGC, Trimby L, Au YY, Nagareddy VK, Rodriguez-Hernandez G, Hosseini P, et al. A nonvolatile phase-change metamaterial color display. *Adv Opt Mater* 2019;7(18):1801782.
- [23] He Q, Youngblood N, Cheng ZG, Miao XS, Bhaskaran H. Dynamically tunable transmissive color filters using ultra-thin phase change materials. *Opt Express* 2020;28(26):39841–9.
- [24] Afínogenov BI, Bessonov VO, Soboleva IV, Fedyanin AA. Ultrafast all-optical light control with Tamm plasmons in photonic nanostructures. *ACS Photonics* 2019;6(4):844–50.
- [25] Buchnev O, Belosludtsev A, Reshetnyak V, Evans DR, Fedotov VA. Observing and controlling a Tamm plasmon at the interface with a metasurface. *Nanophotonics* 2020;9(4):897–903.
- [26] Normani S, Bertolotti P, Bisio F, Magnozzi M, Carboni FF, Filattiera S, et al. Tamm plasmon resonance as optical fingerprint of silver/bacteria interaction. *ACS Appl Mater Interfaces* 2023;15(23):27750–8.
- [27] Ko JH, Seo DH, Jeong HH, Kim S, Song YM. Sub-1-volt electrically programmable optical modulator based on active Tamm plasmon. *Adv Mater* 2024;36(15):2310556.
- [28] Rossi S, Olsson O, Chen S, Shanker R, Banerjee D, Dahlin A, et al. Dynamically tuneable reflective structural coloration with electroactive conducting polymer nanocavities. *Adv Mater* 2021;33(49):2105004.
- [29] Wang Z, Wang X, Cong S, Chen J, Sun H, Chen Z, et al. Towards full-colour tunability of inorganic electrochromic devices using ultracompact fabry-perot nanocavities. *Nat Commun* 2020;11(1):302.
- [30] Yan Z, Zhang Z, Wu W, Ji X, Sun S, Jiang Y, et al. Floating solid-state thin films with dynamic structural colour. *Nat Nanotechnol* 2021;16(7):795–801.
- [31] Liu H, Dong W, Wang H, Lu L, Ruan Q, Tan YS, et al. Rewritable color nanoprints in antimony trisulfide films. *Sci Adv* 2020;6(51):eabb7171.
- [32] Rudé M, Mkhitarian V, Cetin AE, Miller TA, Carrilero A, Wall S, et al. Ultrafast and broadband tuning of resonant optical nanostructures using phase-change materials. *Adv Opt Mater* 2016;4(7):1060–6.
- [33] Mkhitarian VK, Ghosh DS, Rudé M, Canet-Ferrer J, Maniyara RA, Gopalan KK, et al. Tunable complete optical absorption in multilayer structures including Ge₂Sb₂Te₅ without lithographic patterns. *Adv Opt Mater* 2017;5(1):1600452.
- [34] Julian MN, Williams C, Borg S, Bartram S, Kim HJ. Reversible optical tuning of ge-sbte phase-change metasurface spectral filters for mid-wave infrared imaging. *Optica* 2020;7(7):746–54.
- [35] Wuttig M, Lüsebrink D, Wamwangi D, Weinic W, Gilleßen M, Dronskowski R. The role of vacancies and local distortions in the design of new phase-change materials. *Nat Mater* 2007;6(2):122–8.
- [36] Ríos C, Hosseini P, Taylor RA, Bhaskaran H. Color depth modulation and resolution in phase-change material nanodisplays. *Adv Mater* 2016;28(23):4720–6.
- [37] Yoo S, Gwon T, Eom T, Kim S, Hwang CS. Multicolor changeable optical coating by adopting multiple layers of ultrathin phase change material film. *ACS Photonics* 2016;3(7):1265–70.
- [38] Dong WL, Liu HL, Behera JK, Lu L, Ng RJ, Sreekanth KV, et al. Wide bandgap phase change material tuned visible photonics. *Adv Funct Mater* 2019;29(6):1806181.
- [39] Kondrotas R, Chen C, Tang J. Sb₂S₃ solar cells. *Joule* 2018;2(5):857–78.
- [40] Jana S, Sreekanth KV, Abdelraouf OAM, Lin R, Liu H, Teng J, et al. Aperiodic bragg reflectors for tunable high-purity structural color based on phase change material. *Nano Lett* 2024;24(13):3922–9.
- [41] Chen J, Song G, Cong S, Zhao Z. Resonant-cavity-enhanced electrochromic materials and devices. *Adv Mater* 2023;35(47):2300179.
- [42] Johs B. Regression calibration method for rotating element ellipsometers. *Thin Solid Films* 1993;234(1–2):395–8.
- [43] Yee K. Numerical solution of initial boundary value problems involving maxwell's equations in isotropic media. *IEEE Trans Antennas Propag* 1966;14(3):302–7.
- [44] Teo TY, Li N, Tobing LYM, Tong ASK, Ng DKT, Ren Z, et al. Capping layer effects on Sb₂S₃-based reconfigurable photonic devices. *ACS Photonics* 2023;10(9):3203–14.
- [45] Gao K, Du K, Tian S, Wang H, Zhang L, Guo Y, et al. Intermediate phase-change states with improved cycling durability of Sb₂S₃ by femtosecond multi-pulse laser irradiation. *Adv Funct Mater* 2021;31(35):2103327.
- [46] Yang ZY, Ishii S, Yokoyama T, Dao TD, Sun MG, Pankin PS, et al. Narrowband wavelength selective thermal emitters by confined Tamm plasmon polaritons. *ACS Photonics* 2017;4(9):2212–9.
- [47] Lian M, Su Y, Liu K, Zhang S, Chen X, Ren H, et al. Nonvolatile switchable broadband polarization conversion with wearable terahertz chalcogenide metamaterials. *Adv Opt Mater* 2023;11(9):2202439.
- [48] Kelley CK. Thermal analysis study of antimony sulfides. Report. Ohio: Wright Research and Development Center. 1989.
- [49] Massalski TB, Okamoto H, Subramanian PR, Kacprzak L. Binary alloy phase diagrams. Materials Park, OH: ASM International. 1990.
- [50] Mao LB, Li Y, Li GX, Zhang S, Cao T. Reversible switching of electromagnetically induced transparency in phase change metasurfaces. *Adv Photonics* 2020;2(5):056004.
- [51] Song D, Wu B, Liu Y, Wu X, Yu K. A polarization-dependent perfect absorber with high Q-factors enabled by Tamm phonon polaritons in hyperbolic materials. *Phys Chem Chem Phys* 2023;25(37):25803–9.
- [52] Li L, Hao H. Evolution of high-order Tamm plasmon modes with a metal-PHC cavity. *Sci Rep* 2022;12(1):14921.
- [53] Symonds C, Azzini S, Lheureux G, Piednoir A, Benoit JM, Lemaitre A, et al. High quality factor confined Tamm modes. *Sci Rep* 2017;7(1):3859.
- [54] Ferrier L, Nguyen HS, Jamois C, Berguiga L, Symonds C, Bellessa J, et al. Tamm plasmon photonic crystals: from bandgap engineering to defect cavity. *APL Photonics* 2019;4(10):106101.
- [55] Lu H, Shi S, Li D, Bo S, Zhao J, Mao D, et al. $\lambda/20$ -thick cavity for mimicking electromagnetically induced transparency at telecommunication wavelengths. *Adv Photonics* 2024;6(3):036001.
- [56] Chang CC, Chen TY, Lin TW, Leng J, Tamada K, Lee YJ. Flexible and ultranarrow transmissive color filters by simultaneous excitations of triple resonant eigenmodes in hybrid metallic-optical Tamm state devices. *ACS Photonics* 2021;8(2):540–9.
- [57] Wen X, Lu X, Wei C, Li J, Li Y, Yang S. Bright, angle-independent, solvent-responsive, and structurally colored coatings and rewritable photonic paper based on high-refractive-index colloidal quasi-amorphous arrays. *ACS Appl Nano Mater* 2021;4(9):9855–65.
- [58] Lee KT, Ji C, Banerjee D, Guo LJ. Angular- and polarization-independent structural colors based on 1D photonic crystals. *Laser Photonics Rev* 2015;9(3):354–62.